A study of resistive peeling–ballooning modes across spherical tokamaks

OPEN ACCESS
IOP Publishing
Plasma Physics and Controlled Fusion
Plasma Phys. Control. Fusion **67** (2025) 085026 (14pp)
https://doi.org/10.1088/1361-6587/adf91a

A study of resistive peeling–ballooning modes across spherical tokamaks

A Kleiner[1,*], K Imada[2,3], F Ebrahimi[1], N M Ferraro[1], S R Haskey[1], L Kogan[4] and A Pankin[1]

[1] Princeton Plasma Physics Laboratory, PO Box 451, Princeton, NJ 08543-0451, United States of America
[2] General Atomics, San Diego, CA 92186-5608, United States of America
[3] York Plasma Institute, School of Physics, Electronics and Engineering, University of York, Heslington, York YO10 5DD, United Kingdom
[4] UKAEA, Culham Campus, Abingdon, Oxon OX14 3DB, United Kingdom

E-mail: akleiner@pppl.gov

Received 31 March 2025, revised 8 July 2025
Accepted for publication 7 August 2025
Published 20 August 2025

Abstract

We investigate how non-ideal-magnetohydrodynamics (MHD) effects, in particular plasma resistivity, impact the peeling–ballooning stability thresholds in spherical tokamaks. This analysis follows the discovery of resistive kink-peeling modes in ELMing National Spherical Torus Experiment (NSTX) discharges. In the present study we extend this modeling to ELMing pulses in the Mega Ampere Spherical Tokamak (MAST) and MAST—Upgrade (MAST-U), where we find a clear resistive scaling for peeling–ballooning modes. While in NSTX ideal-MHD predicts stability for ELMing discharges, in MAST-U we find that the plasma is slightly unstable to peeling–ballooning modes, but is fully stabilized once diamagnetic effects are considered in terms of a growth rate normalization. A resistive power law scaling is calculated for these modes on MAST-U, which lies in between that of tearing modes and resistive interchange modes. A comparison between M3D-C1 and NIMROD shows reasonable agreement for this scaling. Resistivity destabilizes the modes and the peeling–ballooning unstable domain is considerably expanded in both, MAST and MAST-U. In addition to the MAST/-U pulses we also analyze resistive PB stability in a NSTX-similarity discharge on DIII-D. While having a different aspect ratio from NSTX, this discharge uses NSTX-like shaping parameters, toroidal field and plasma current. By considering these discharges alongside NSTX cases, we identify conditions influencing the onset of resistive peeling–ballooning modes. Our findings indicate that magnetic shear in the pedestal region is closely linked to the emergence of resistive edge modes.

Keywords: magnetohydrodynamics, MAST-U, peeling–ballooning, edge localized modes, pedestal, spherical tokamak

* Author to whom any correspondence should be addressed.

1. Introduction

Edge-localized modes (ELMs) have been known to constitute a major challenge for the operation of reactor-scale tokamaks [1], and their control and avoidance is of crucial importance. Current tokamak experiments provide a good platform for understanding the onset of ELMs and developing models to describe the underlying physics and predict ELM-free regimes. For some machines such as DIII-D and other large aspect ratio tokamaks ideal peeling–ballooning (PB) modes explain the occurrence of type-I ELMs sufficiently well [2]. However, some scenarios have been described where this is not the case [3–7], and higher fidelity models are required. Recent modeling with extended-magnetohydrodynamics (MHD) models has been performed and identified that plasma resistivity can explain ELM stability limits in the National Spherical Torus Experiment (NSTX) [8–10] and JET-ILW [11] scenarios. Further work has revealed the importance of non-ideal effects on PB stability [12]. Nonlinear simulations of ELMs have also been performed in the past with different codes [13–15]. It is therefore important to understand in which parameter regimes such resistive PB MHD modes are associated with type-I ELMs as this can facilitate the prediction of ELM-free scenarios and aid in scenario development for future devices.

It is still unclear whether tokamaks besides NSTX and JET-ILW are prone to developing resistive PB instabilities. An ideal-MHD peeling–ballooning stability study with the ELITE code showed that ELMing discharges in the Mega Ampere Spherical Tokamak—Upgrade (MAST-U) are located close to the peeling–ballooning stability threshold [16]. An open question in this study remained about how to define the stability threshold for these plasmas. In ideal-MHD the transition from stability to instability happens at a normalized growth rate of $\gamma/\omega_{\rm A} = 0$, where γ is the ideal-MHD growth rate and $\omega_{\rm A}$ is the Alfvén frequency. However, for the presented MAST-U pulses the stability limit had to be set at slightly larger, finite values of $\gamma/\omega_{\rm A}$. While these adjusted thresholds effectively captured the stability characteristics of the discharges, it is an indication that additional physical effects may influence ELM stability thresholds on MAST-U. One such effect could be plasma resistivity, which was previously found to destabilize peeling–ballooning modes in NSTX [8–10] and JET-ILW [11]. Since MAST and MAST-U feature a similar aspect ratio as NSTX and operate with comparable magnetic field strength, it is worth investigating whether these spherical tokamaks (STs) also exhibit such resistive edge modes.

In this paper we present extended-MHD simulations with the M3D-C1 code [17] to calculate the resistive peeling–ballooning stability threshold of a MAST and a MAST-U pulse with single-fluid extended MHD models and in the ideal-MHD limit. In the context of this paper, 'extended-MHD' refers to any MHD model that includes effects beyond the ideal-MHD model, e.g. plasma resistivity, plasma viscosity, etc. The exact model used in the presented simulations, is described in section 2. To increase confidence in the results a comparison with the NIMROD code [18] is performed. We also include toroidal plasma rotation to understand whether equilibrium rotation can influence peeling–ballooning stability. For this analysis, we use the available rotation profiles from experimental measurements in the given pulses. Our goal is to provide a preliminary assessment of whether equilibrium rotation plays a significant role. PB stability analysis including equilibrium rotation is rarely performed. And while few studies exist on conventional tokamaks that include equilibrium rotation [12, 19], the influence of rotation on macroscopic edge modes remains an uninvestigated problem on STs. Another goal of this paper is to determine plasma conditions that are associated with the occurrence of resistive peeling–ballooning modes. To broaden the parameter space, we also include a DIII-D discharge with NSTX-like parameters.

This paper is structured as follows: section 2 describes the extended-MHD model adopted in the M3D-C1 code. Section 3 investigates linear PB mode stability in MAST and MAST-U, including the sensitivity of edge modes to resistivity and calculation of the stability boundary w.r.t. the experimental point. It also provides a short comparison with the NIMROD code. A discussion of the physics associated with the occurrence of resistive PB modes in different tokamaks is presented in section 4. This includes a discharge in DIII-D with some NSTX-like parameters.

2. Calculation of edge stability limits with M3D-C1

2.1. Physical model & numerical approach

Since our goal is to extend our previous study of the effect of plasma resistivity from NSTX to other STs, we employ the same physical model using the M3D-C1 initial value stability code. M3D-C1 uses an extended-MHD model that is derived from the Braginskii equations. In particular, in this study we adopt a set of single-fluid extended-MHD equations that include the effects of resistivity, viscosity as well as particle and thermal diffusivity. We employ the following set of equations:

$$\begin{aligned}
\frac{\partial n_{\rm s}}{\partial t} + \nabla\cdot(n_{\rm s}\mathbf{u}) &= \Sigma\,,\\
m_{\rm i} n_{\rm s}\left(\frac{\partial \mathbf{u}}{\partial t} + \mathbf{u}\cdot\nabla\mathbf{u}\right) &= \mathbf{J}\times\mathbf{B} - \nabla p - \nabla\cdot\Pi - m_{\rm i}\mathbf{u}\Sigma\,,\\
\frac{\partial p}{\partial t} + \mathbf{u}\cdot\nabla p + \Gamma p\nabla\cdot\mathbf{u} &= (\Gamma-1)\left[\eta J^2 - \nabla\cdot\mathbf{q}\right.\\
&\qquad \left. -\Pi:\nabla\mathbf{u} - \frac{1}{2}m_{\rm i}v^2\Sigma\right]\,,\\
\mathbf{E} &= -\mathbf{u}\times\mathbf{B} + \eta\mathbf{J}\,,\\
\mathbf{J} = \frac{1}{\mu_0}\nabla\times\mathbf{B} \quad &, \quad \frac{\partial\mathbf{B}}{\partial t} = -\nabla\times\mathbf{E}\,,
\end{aligned} \tag{1}$$

with $\Sigma := D\nabla^2 n_{\rm s}$ and where, $n_{\rm s} = n_{\rm i} = n_{\rm e}$ is the particle density of the electron and ion species, $\mathbf{u}$ the fluid velocity, $\mathbf{B}$ the magnetic field, p the pressure, $\mathbf{J}$ the current density, $\mathbf{E}$ the

electric field, η the resistivity, $\Pi = -\mu[\nabla \mathbf{u} + (\nabla \mathbf{u})^t]$ the viscous stress tensor, $\mathbf{q} = -\kappa \nabla T - \kappa_{\|} \widehat{\mathbf{bb}} \nabla T$ the heat flux density, $\Gamma = 5/3$ the adiabatic index, m_i the ion mass, D denotes particle diffusivity κ the isotropic heat conductivity, $\kappa_{\|}$ the parallel heat conductivity, $\widehat{\mathbf{b}}$ the unit vector in direction of the magnetic field and μ is the isotropic viscosity [20]. This system of equations is solved in M3D-C1 using C^1 finite elements [17, 21] on an unstructured triangular mesh. The mesh is adapted for each equilibrium, such that the mesh elements align with the flux surfaces. This ensures high resolution in the pedestal region and lower resolution in other parts of the computational domain. Since equations (1) constitute a single fluid-model, i.e. there is only one bulk fluid velocity $\mathbf{u}$, diamagnetic rotation is not naturally included in the system of equations that is solved in the present analysis. While the code is capable of including diamagnetic effects in the full two-fluid model, this treatment is reserved for future work as it introduces additional numerical and physical challenges. Plasma resistivity is calculated according to the well-known Spitzer resistivity model. Due to the requirement of quasi-neutrality ($n_\mathrm{i} = n_\mathrm{e}$) in MHD calculations, and because the total pressure p is specified in addition to n_e and electron temperature T_e, the main ion temperature is determined by these quantities as $T_\mathrm{i} = p/n_\mathrm{e} - T_\mathrm{e}$. The T_e and T_i profiles are comparable in magnitude and thus calculation of the resistivity profile from T_e is justified. Note that in our model we use a Spitzer resistivity profile without neoclassical or Z_eff corrections. However, the expected neoclassical correction to the Spitzer resistivity profile would be approximately a factor of 2, which lies within the range of scaled resistivity values in our study. Based on the results of our resistivity scan we expect these corrections to the Spitzer profile to be further destabilizing. At the same time the single-fluid MHD model ignores some stabilizing effects that would be expected in a full two-fluid MHD model, such as gyroviscosity and Hall effects. We would thus expect that these effects would counteract the destabilizing effect of the corrected resistivity profile. The magnitude of these contributions is to be explored in future work. Because finite values of resistivity are required in M3D-C1, we take the ideal-MHD limit to be at 10% of Spitzer resistivity. This limit is justified since the growth rate remains nearly constant below this threshold as laid out in [22] and confirmed with linear M3D-C1 simulations on NSTX. In our model the stress tensor Π includes the effect of finite viscosity, which has a direct influence on the growth rate. It is difficult to determine the exact value of viscosity in a fusion plasma. However, by investigating the sensitivity of the PB mode growth rate on viscosity it was determined that within the range of realistic viscosity values the growth rate does not vary strongly. Hence, choosing a realistic value for viscosity is expected to result in accurate stability thresholds. We choose a value of $2.577\,735\,22 \times 10^{-7}\,\mathrm{kg\,m^{-1}s^{-1}}$. This is within the range of viscosity values of about $1.0\times 10^{-7}\,\mathrm{kg\,m^{-1}s^{-1}}$ to $2.5\times 10^{-6}\,\mathrm{kg\,m^{-1}s^{-1}}$ that is typically used in M3D-C1 and other extended-MHD simulations [23]. Equilibrium rotation can be included in two ways: 1) By including a centrifugal term in the Grad–Shafranov equation. 2) By solving the regular Grad–Shafranov equation without this term and initializing the initial fluid velocity field based on a given rotation profile. Here, we choose the latter approach as the centrifugal term in the Grad–Shafranov equation often introduces numerical challenges, which is unpractical for running a large amount of simulations as shown in this paper.

In the M3D-C1 simulations $f = RB_\phi = 0$ on the boundary, which implies $\widehat{\mathbf{t}} \cdot \nabla f = 0$ along the boundary. Additional boundary conditions are set to prevent normal flow, poloidal flow and toroidal flow at the boundary. In all of the presented simulations the boundary is sufficiently far away from the plasma such that the density is negligible, i.e. the amount of plasma at the boundary is small enough that potential flows along the boundary would not be expected to have an effect on mode stability in the pedestal. We would also like to emphasize that the mode perturbation in the presented cases does not extend to the plasma boundary.

In linear simulations the toroidal modes are decoupled and simulations are carried out for each n individually. The growth rate is determined as $\gamma = \frac{1}{2}\mathrm{d}/\mathrm{dt}\ln(E_\mathrm{kin})$, where E_kin is the plasma kinetic energy. Since initial value simulations, like those we perform with M3D-C1, will pick up any type of unstable mode anywhere in the plasma, an analysis of mode types is performed to distinguish PB modes from other types of instabilities. The modes are characterized in terms of their eigenfunction by evaluating radial and poloidal location, poloidal mode spectrum and their sensitivity to certain physical effects that drive the instability. In the remainder of this paper, $\psi_\mathrm{N} = (\psi - \psi_0)/(\psi_1 - \psi_0)$ denotes the normalized poloidal flux. Here, ψ_0 and ψ_1 are the poloidal flux at the magnetic axis and the separatrix, respectively. As in previous analysis, we adopt the same simple model of diamagnetic stabilization as in ELITE [24]. This allows for a better comparison with ideal-MHD studies and our previous work on NSTX [8, 9]. With this normalization the stability boundary is given as $\gamma/(\omega_{*i}/2) = 1$. The plasma is considered stable if $\gamma/(\omega_{*i}/2) < 1$ and unstable if $\gamma/(\omega_{*i}/2) > 1$, where γ is the mode growth rate and ω_{*i} is the effective ion diamagnetic frequency in the pedestal. Since the ion diamagnetic frequency varies strongly in the pedestal region, an effective diamagnetic frequency ω_{*i} is chosen for the normalization. It is defined as half of the maximum value of the ion diamagnetic frequency inside the pedestal. This is the same approach as in ELITE and enables a better comparison [24]. A constant approximation for ω_{*i} instead of retaining a radially varying ω_{*i} can affect the magnitude of the diamagnetic stabilization [25, 26].

3. Stability analysis in MAST and MAST-U

To better understand the role of plasma resistivity on ELM stability thresholds in STs beyond NSTX, we now expand our analysis to MAST and MAST-U. We first determine the resistive scaling in ELMing pulses of these two machines and then calculate the PB stability thresholds for a discharge in each

device using ideal and resistive MHD models. In this section, linear stability simulations are carried out for these pulses with toroidal modes ranging from $n = 1 - 40$. To determine the resistive scaling all toroidal modes $\leqslant 40$ are considered, but for the calculation of the stability boundaries we choose a step size of of 3, i.e. $n = 1, 4, 7, 10, \ldots, 40$. We increased the maximum value of n compared with previous NSTX simulations, because ELITE simulations have shown larger toroidal mode numbers to be important on MAST/-U [16, 27]. The step size of 3 is chosen as a trade-off between capturing many toroidal modes and reasonable computational cost for the simulations.

3.1. Plasma equilibrium

The first equilibrium considered in the present analysis is for MAST-U pulse 45 272 at time 477 ms. This discharge exhibits type-I ELMs and was recently studied [16] using the ideal-MHD code ELITE. (Partial) kinetic equilibrium reconstructions on MAST and MAST-U are typically being performed with the EFIT++ Grad–Shafranov solver [28]. Because such EFIT++ [29] equilibrium calculations can exhibit inconsistent pressure profiles at the plasma edge, i.e. it is not guaranteed that $p \geqslant p_e + p_i$ (impurities and fast particles can also contribute to the total thermal pressure). A workflow was employed to ensure that p is the sum of the partial pressure contributions. The kinetic EFIT was obtained through the kineticEFITtime OMFIT [30, 31] module using EFIT++ as equilibrium solver. In a next step the total pressure was recalculated from the species' particle pressures and a new Grad–Shafranov equilibrium was calculated with the fixfit code, a fixed-boundary equilibrium solver. fixfit was also used to calculate the equilibria with scaled pressure and current profiles through VARYPED [32]. For more details regarding the VARYPED workflow we refer to [16]. The equilibrium that are obtained in this manner, are calculated only up to the last closed flux surface and the poloidal flux is extrapolated by fixfit to fill a rectangular computational box that is only marginally larger than the plasma itself. Such a small computational box does not fully cover the computational domain required for simulations with M3D-C1. To address this limitation the equilibrium is recalculated with the CHEASE equilibrium solver [33]. This yields an essentially identical equilibrium within the last closed flux surface while extending the flux field outward to ensure a sufficiently large computational domain. Since M3D-C1 can model vessel components as conductors with realistic resistivities, we usually try to include the inner wall in the computational domain using an appropriate resistivity value. However, because the MAST and MAST-U equilibria had to be recalculated with a fixed-boundary solver, the computational domain of the input equilibrium was not large enough to fit the device wall of either MAST or MAST-U into the domain. Hence, the inner wall is omitted from the simulations. In these cases the M3D-C1 computational domain acts as an ideal wall, and is kept at roughly the same distance as the actual device walls of MAST and MAST-U. Such a wall distance is expected to not considerably affect peeling stability [34].

The second equilibrium considered here is for MAST (prior to the upgrade) pulse 29 782 at time 446 ms. Similar to the MAST-U case described above, this is a typical H-mode pulse with type-I ELMs. The equilibrium has been reconstructed with the EFIT++ equilibrium solver. Unlike in the MAST-U case the total pressure profile was consistent with the sum of the reconstructed electron pressure p_e and ion pressure p_i profiles, eliminating the need to compute a new Grad–Shafranov solution. Nevertheless, to calculate the equilibrium variation with VARYPED it was necessary to again employ fixfit, and thus process the varied equilibria with CHEASE as described above.

Equilibrium shape and the profiles for electron density n_e, electron temperature T_e, total pressure p and flux-averaged toroidal current density $< j_\phi >$ for the MAST and MAST-U equilibria are shown in figure 1.

3.2. Resistive peeling–ballooning growth rates

We now determine the sensitivity of the PB mode growth rate w.r.t. plasma resistivity η in the MAST and MAST-U discharges using the kinetic equilibria described above. η is calculated based on the Spitzer resistivity model and scaled in a range from $0.1 - 10$. The mode growth rates at different plasma resistivities are compared in figure 2 using two different normalizations for the growth rate γ. The modes in both pulses show a dependence on resistivity, however, between the ideal-MHD limit and twice the Spitzer resistivity value it is much weaker than what was previously seen in NSTX [8, 9]. When increasing the resistivity profile from regular Spitzer resistivity to twice its value, the growth rate roughly doubled on ELMing NSTX discharges, whereas on the investigated MAST/-U pulses it only increases by a factor of about 1.2, as seen in figure 2. The resistive scaling is further quantified in section 3.3. When γ is normalized w.r.t. the Alfvén frequency ω_A the growth rate increases with toroidal mode number n for all considered values of resistivity. While ELMing NSTX plasmas appeared to be fully stable ($\gamma/\omega_A < 0$), the considered MAST and MAST-U discharges appear unstable already for $n = 1$ and $n \geqslant 8$ in the ideal-MHD limit ($\eta_S \times 0.1$) when the same stability criterion of $\gamma/\omega_A = 0$ is applied. This is the key difference to the NSTX observations [8]. Another commonly used normalization for PB modes considers the ion diamagnetic frequency in the pedestal ω_{*i} as explained in section 2. This normalization has two advantages: it provides a simple physical model to include diamagnetic stabilization [35] and at the same time provides a physically justified stability threshold of $\gamma/(\omega_{*i}/2) = 1$ that can eliminate slightly unstable modes, which are often seen in resistive MHD simulations, but grow so slowly that they would not be associated with the explosive nature of ELMs. With this normalization the MAST pulse appears PB-unstable in the ideal-MHD limit, but the MAST-U pulse stays underneath the stability limit of $\gamma/(\omega_{*i}/2) = 1$ and would be considered stable.

The $n = 1$ growth rate in MAST pulse 29 782 corresponds to a pure core mode, which could to be similar to the long-lived mode that has been described in many MAST

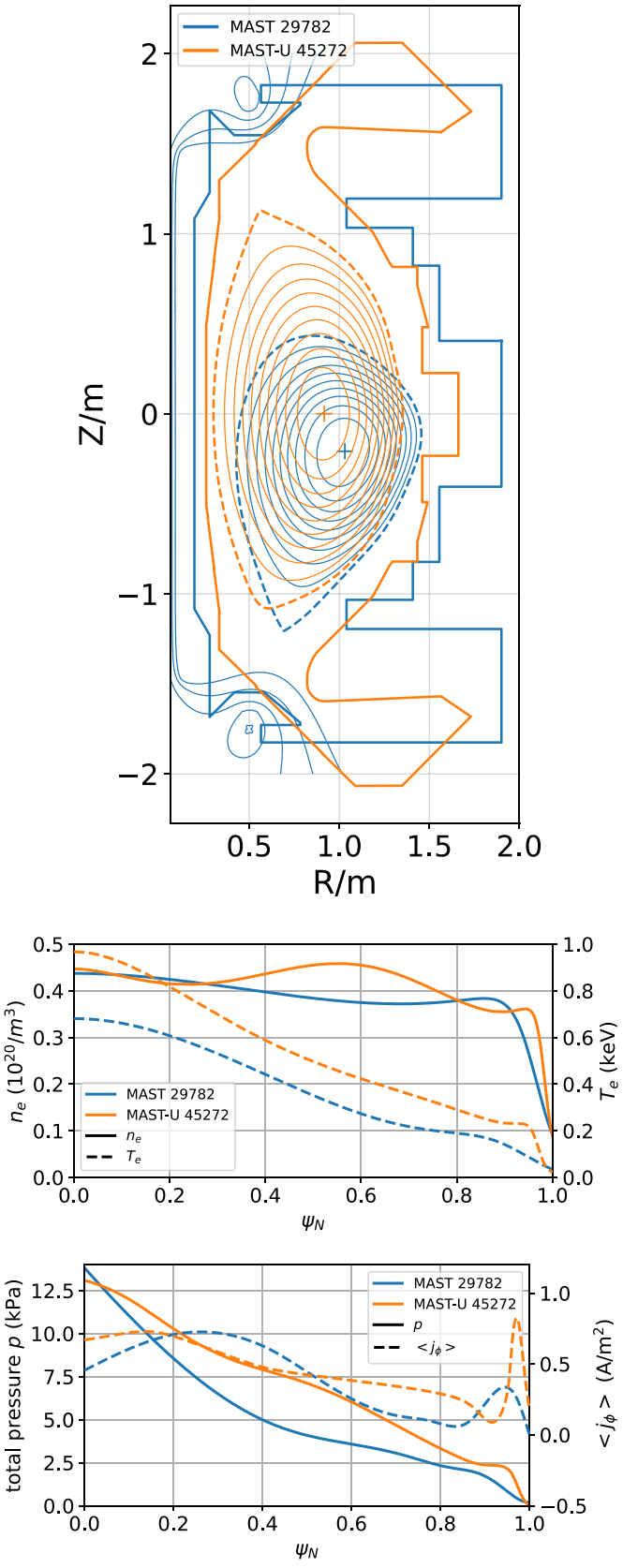

Figure 1. Equilibrium of the MAST and MAST-U pulses used for peeling–ballooning stability analysis. (top) Flux surfaces (lcfs is shown bold), magnetic axis (+) and first wall. (middle) electron density n_e and electron temperature T_e. (bottom) Total pressure p and flux-averaged toroidal current density j_ϕ.

experiments [36, 37]. Unlike the edge modes at $n > 1$, this core mode shows no destabilization with increasing resistivity, suggesting that it is an ideal instability. In the MAST-U pulse we do not find such an ideal core mode. Nevertheless, soft x-ray spectra reveals a core mode in the experiment [16], which could be explained by including resistivity. The magnitude of this core mode is, however, determined by the nonlinear evolution of the instability and growth rates alone do not necessarily provide insight on how strong the experimentally observed mode would be.

3.3. Characterizing the resistive scaling with M3D-C1 and NIMROD

In this section we determine the resistive scaling of resistive peeling–ballooning modes in terms of the Lundquist number $S = Lv_A/\eta$, where L is the typical length scale of the system, v_A is the Alfvén velocity and η is resistivity. In order to increase confidence in the resistive nature of these instabilities, linear stability simulations are also carried out with the NIMROD code [18] and compared with the M3D-C1 computations. We have initiated linear code comparisons between M3D-C1 and NIMROD for PB modes without equilibrium flows for the time being. For this initial code comparison of extended-MHD simulations on modes in the edge pedestal MAST-U pulse 45 272 is chosen, and the focus is on a linear resistivity scan within an extended-MHD model similar to the one used in M3D-C1. While both codes employ an extended-MHD model that is derived from the Braginskii equations, a major difference in terms of the physics model concerns the implementation of diffusive processes. M3D-C1 uses a constant thermal conductivity κ, whereas NIMROD uses a constant thermal diffusivity $\chi = \kappa/n_s$ (where $n_s = n_e = n_i$ is the particle density). A similar difference exists for the isotropic viscosity, which in M3D-C1 is directly specified with dimensions of mass / (length · time) and held constant, whereas in NIMROD a diffusivity with dimensions of length^2/time is held constant, which differs from the constant viscosity in M3D-C1 by a factor of mass density ρ. The NIMROD simulations were performed with uniform particle and thermal diffusivity profiles set to $1\,\mathrm{m^2 s^{-1}}$ and parallel viscosity fixed at $1 \times 10^5\,\mathrm{m^2 s^{-1}}$. Simulations were performed for the whole plasma domain including the scrape-off-layer (SOL) without two-fluid effects. The computational grid is varied in the poloidal direction from 126 to 504 grid points, depending on the mode number, while the radial resolution is maintained at 72 grid points with a polynomial degree of 5. These settings ensure adequate resolution for capturing the linear growth of MHD instabilities driving ELMs in the MAST-U tokamak with high values of q in the plasma edge.

In order to quantify the resistive scaling of resistive PB modes we calculate a power law of the form aS^b by fitting the growth rates γ/ω_A at different resistivity values for given toroidal mode numbers. Here, S is the Lundquist number and a, b are fitting parameters. Figure 3(a) shows the growth rates γ/ω_A as a function of S for $n = 10, 12, 15, 18, 20$ calculated with M3D-C1 and NIMROD. A clear destabilization of PB

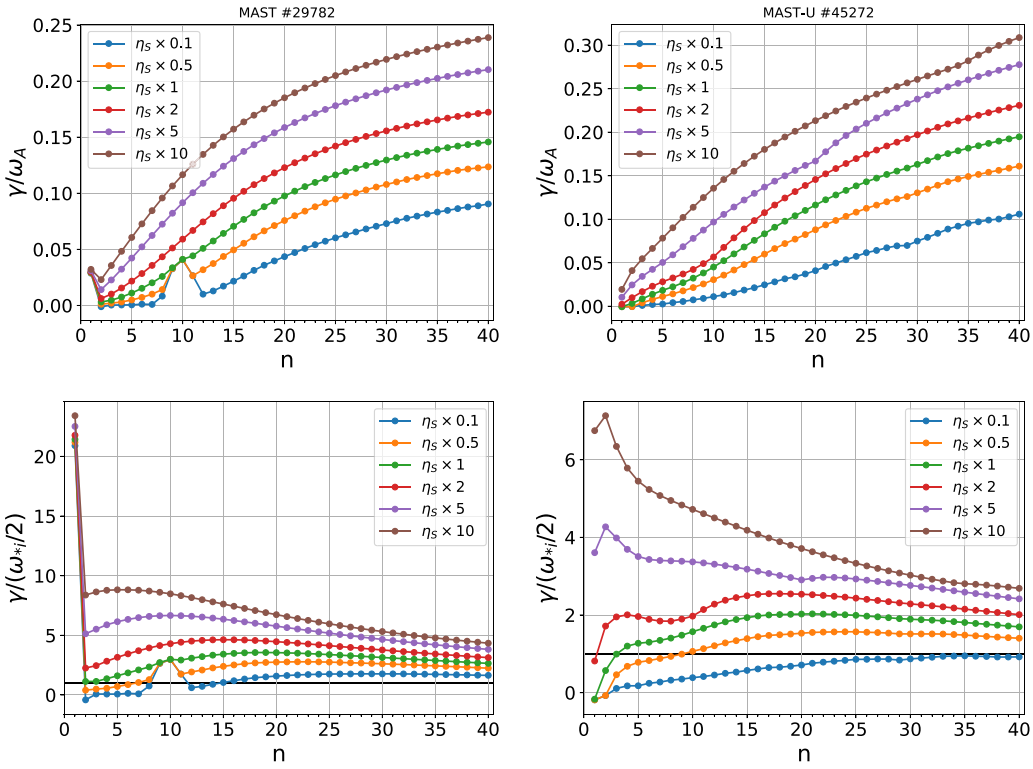

Figure 2. The mode growth rate γ/ω_A as a function of toroidal mode number n at varying values of resistivity. A Spitzer resistivity profile η_S is used and scaled by factors in the range of $0.1 - 10$. (left) MAST 29 782. (right) MAST-U 45 272. The horizontal black line shows the stability threshold $\gamma/(\omega_{*i}/2) = 1$.

modes with resistivity is found in NIMROD similar to M3D-C1. Overall, M3D-C1 shows a stronger decrease of the resistive scaling with increasing n than NIMROD does, i.e. M3D-C1 shows $\gamma \propto S^{-0.513}$ for $n = 10$ and $\gamma \propto S^{-0.302}$ for $n = 20$, whereas NIMROD provides a somewhat slower scaling at $n = 10$ of $\gamma \propto S^{-0.410}$ and a slightly faster scaling than M3D-C1 for $n = 20$ of $\gamma \propto S^{-0.345}$. Nevertheless, in both codes the calculated scalings lie in approximately the same range and are slower than that of tearing modes ($\gamma \propto S^{-0.6}$) and faster than that of resistive interchange modes ($\gamma \propto S^{-3/13}$). The resistive scaling in MAST pulse 29 782 was calculated with M3D-C1 and is similar to that of the MAST-U pulse. Figure 3(b) compares the resistive scaling seen on MAST-U #45272 with the scaling of resistive kink-peeling modes that was previously observed on NSTX [9]. Whereas the exponent in the power law decreases with n on the investigated MAST-U discharge, it increases for the resistive kink-peeling modes seen on NSTX, but otherwise they cover a similar range. However, in the NSTX case the exponent was calculated only by fitting the growth rates in the range from $S = 3 \times 10^5$ to $S = 8 \times 10^6$, because for higher values of S the resistive scaling deviates from the power law. If those points were included, the overall scaling would be faster on NSTX than it is on MAST-U. It can also be asserted that between $S = 1 \times 10^7$ and $S = 1 \times 10^8$ the modes in NSTX are much more sensitive to resistivity than on MAST-U. In fact, for high values of S the growth rate γ/ω_A becomes negative on NSTX, whereas it remains positive on MAST-U. This prohibits the calculation of a scaling law of the typical form aS^b for NSTX.

3.4. Extended-MHD PB stability boundaries

Equilibria with varied pedestal pressure and current density are now used for linear stability simulations to determine the PB stability thresholds relative to the experimental points in MAST #29782 and MAST-U #45272. The simulations are performed with resistive MHD and in the ideal-MHD limit at 10% of Spitzer resistivity. Furthermore, the stability boundary is calculated both without equilibrium rotation and with a given rotation profile. However, the approach for the rotation profile differs between the two discharges. For the MAST discharge we do not have a measured toroidal rotation profile and the simulations can only use the diamagnetic term of the $E \times B$ flow $\omega_{E\times B}$, as this can be calculated from the available profiles. For the MAST-U discharge a set of rotation profiles is available based on measurements of carbon rotation. In these reconstructed profiles the diamagnetic term for the main ions does, however, show a strong and narrow peak close to the LCFS, which appears unphysical, and thus the diamagnetic term $\frac{\mathrm{d}p_C}{\mathrm{d}\psi}/(6n_C)$, in the $E \times B$ rotation profile is not considered in the MAST-U discharge. Here, p_C and n_C are the measured carbon impurity pressure and density, respectively. Figure 4 shows the rotation profiles used in the simulations. Due to limitations with the equilibrium reconstruction on MAST and MAST-U on the given pulses, the rotation profiles for the two cases were obtained in different ways and differ qualitatively. The ion $E \times B$ profiles obtained in the equilibrium reconstruction are consistent with realistic radial electric field E_r profiles. While we strive to use the full

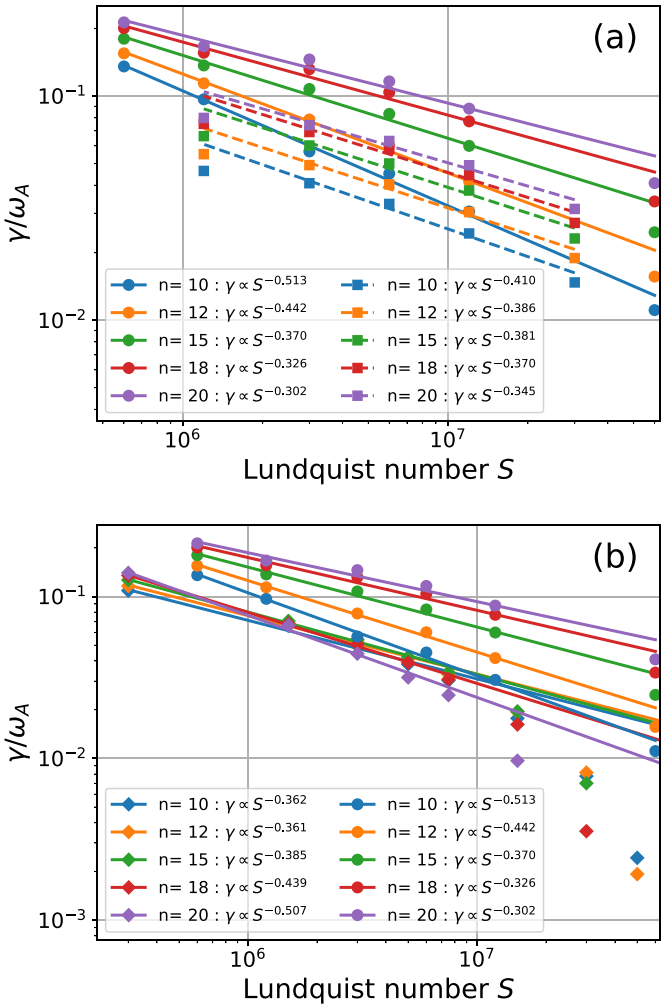

Figure 3. (a) Resistive peeling–ballooning mode growth rate as a function of the Lundquist number S calculated with M3D-C1 (circles) and NIMROD (squares) for different toroidal mode numbers n for MAST-U #45272. A scaling law of the form aS^b is fitted to the M3D-C1 results (solid lines) and to the NIMROD results (dashed lines). (b) Comparison of resistive scalings in NSTX #132543 (diamonds, dotted lines) and MAST-U #45272 (circles, solid lines) calculated with M3D-C1.

ion $E \times B$ rotation profiles whenever possible, there are practical limitations in some cases, which is why the MAST and MAST-U profiles each use only part of the full $E \times B$ rotation profile. Despite this limitation the magnitude of the toroidal rotation is comparable in between all three cases. Note that the goal of this study is only to provide some insight into whether the presence of equilibrium rotation can affect the PB stability boundaries, since this is still an open question. Because we employ a single-fluid model in M3D-C1 as given by equation (1), there is only one toroidal bulk fluid velocity with zero poloidal velocity. The normalization $\gamma/(\omega_{*i}/2)$ can thus still be applied without accounting for diamagnetic stabilization twice. Figure 4 also shows the rotation profile of a DIII-D discharge that is analyzed in section 4.1. A more detailed analysis of how plasma rotation can impact PB stability is currently under investigation.

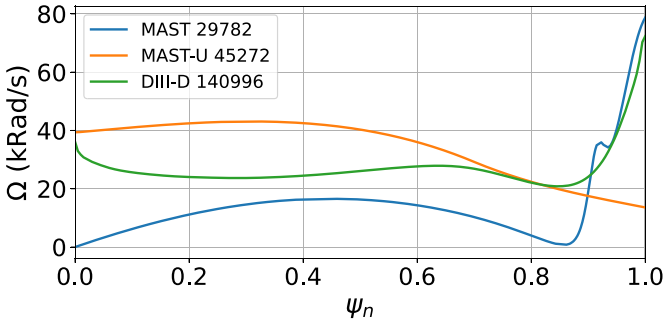

Figure 4. Reconstructed rotation profiles for MAST #29 782, MAST-U #45 272 and DIII-D #140 996. These profiles are used in M3D-C1 to initialize the fluid velocity in the equilibrium. The profile shown for DIII-D is the main ion $E \times B$ velocity, for MAST 29 782 the diamagnetic contribution to the $E \times B$ velocity, and for MAST-U 45 272 it is the main ion $E \times B$ velocity profile without the diamagnetic term.

While the stability of ideal peeling–ballooning modes in the presence of equilibrium rotation has not yet been thoroughly explored, previous studies of resistive peeling–ballooning modes on NSTX were carried out with equilibrium rotation included [8, 9]. This was done because in NSTX plasma rotation stabilizes core modes at intermediate n that make it difficult to isolate edge modes in linear simulations. In contrast, apart from the $n = 1$ core mode in MAST, which has a much smaller growth rate than most higher-n modes, such core modes are not observed in the MAST/-U discharges investigated here, thus enabling a direct comparison of PB stability thresholds both with and without the inclusion of some form of equilibrium rotation. It also allows us to determine whether rotation affects ideal PB modes, resistive PB modes, or both.

First, we focus on pre-upgrade MAST pulse 29 782. The PB stability boundaries calculated with and without equilibrium rotation and using the ideal-MHD limit as well as resistive MHD are presented in figure 5. A moderate increase of the growth rate γ is observed when Spitzer resistivity is introduced. This is true for both, the cases with and without equilibrium rotation. In all four cases γ exhibits a strong dependency on pressure gradient, but not on current density. Together with the fact that the perturbation is localized in the bad curvature region it can be asserted that this MAST pulse is limited by ballooning modes. The only moderate shift of the stability boundary with Spitzer resistivity is similar to that seen in a type-I DIII-D discharge that was used as a benchmark to test our resistive PB model [8]. The results show that resistivity has only a marginal effect on the stability limits in this MAST discharge and hence ideal-MHD describes PB stability sufficiently well. This is in line with previous studies that investigated PB stability on MAST prior to the upgrade and found that ideal-MHD models can reasonably well describe the occurrence of ELMs [27, 38, 39]. When comparing the growth rates and location of the stability boundary at $\gamma/(\omega_{*i}/2) = 1$ between the cases with and without equilibrium flows in figure 5 it is seen that rotation has a somewhat ambiguous effect on stability. On the one hand it moves the stability threshold towards higher values of

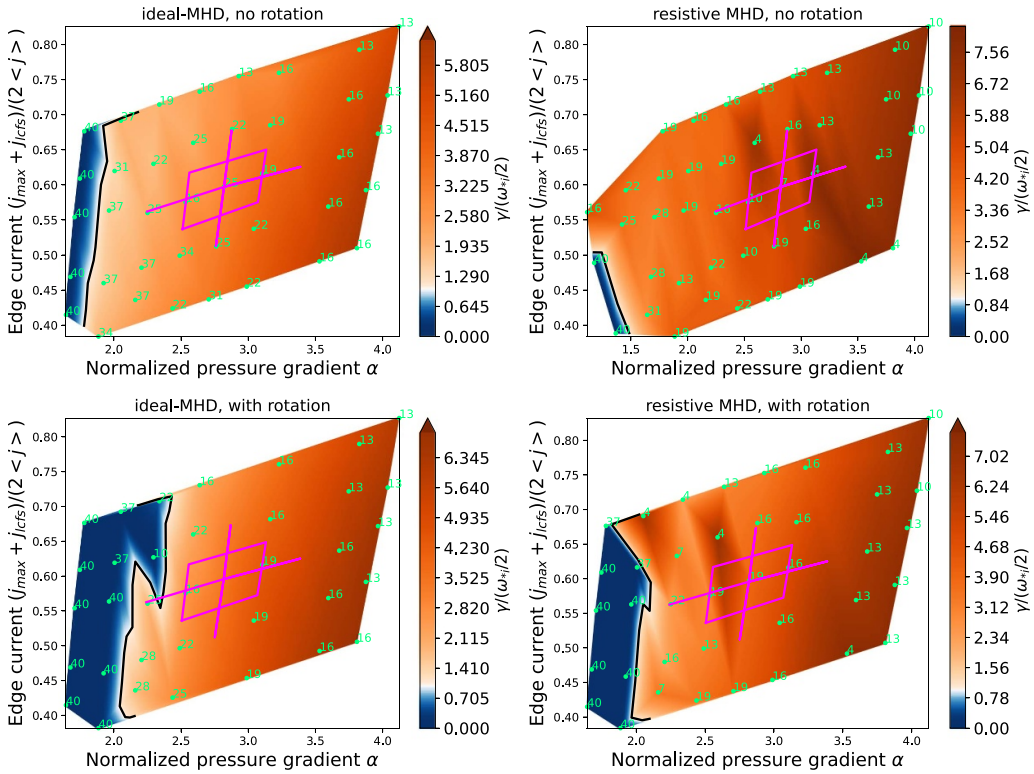

Figure 5. Peeling–ballooning stability boundary and normalized growth rate $\gamma/(\omega_{*i}/2)$ of the most unstable mode calculated for MAST pulse 29 782. The top row shows the results without equilibrium rotation, and the bottom row using a rotation profile based on the diamagnetic term (blue curve in figure 4). (left) ideal-MHD. (right) resistive MHD (Spitzer resistivity). Note that the top right figure uses a larger range of α compared to the other figures such that the stability threshold can be captured.

the normalized edge pressure gradient α, and thus acts stabilizing, but on the other hand it increases the mode growth rate at high values of edge pressure (i.e. large α) by about 10% and acts destabilizing in this part of parameter space in the ideal-MHD model. However, in the resistive model rotation acts stabilizing across the domain. Note that the most unstable modes are in the range of $n = 13 - 16$, and are comparable at large α independent of whether rotation is included or not. This result could indicate that the effect of rotation on PB stability is rather complex and could go beyond being overall stabilizing or destabilizing. Further studies are necessary to assert how plasma equilibrium flows affect macroscopic edge stability.

Next, figure 6 shows the stability boundary in MAST-U #45272 calculated with the same models that were employed for MAST #29782. In the ideal-MHD calculations the experimental equilibrium is located close to a ballooning stability threshold, but still on the stable side. This is not too different from earlier ideal-MHD ELITE computations, where a different growth rate normalization and criterion for the stability threshold were used [16]. When equilibrium rotation is considered, the ideal-MHD stability threshold remains essentially unchanged. The PB growth rates are not affected considerably by rotation either, which indicates that at least in this case ideal peeling–ballooning stability is not impacted by equilibrium rotation. The shape of the stability boundary here is comparable to the ELITE calculations in [16] and indicates that the discharge is located more on the ballooning side than the kink-peeling side. The experimental point and the error bars are, however, completely on the stable side, which indicates that the discharge should be stable to ELMs. Note that MAST #29782 has not been investigated with ELITE. Due to the overall challenges of using the conventional ELITE code on low aspect ratio equilibria [40] and non-availability of the low aspect ratio version of ELITE, performing ELITE simulations and comparing those to M3D-C1 is out of scope of the current study. When Spitzer resistivity is introduced, the unstable domain increases in size significantly and now encloses the experimental point—and in contrast to the ideal-MHD calculation—indicating instability to ELMs. This increase of the unstable domain is similar to what was seen previously in ELMing NSTX discharges [8]. However, the resistive modes in the MAST-U discharge do not exhibit a strong and clear sensitivity to current density as the modes in NSTX. The resistive instabilities here have features of ballooning modes, which can also be resistive in nature [41]. Due to the relatively weak gradient of the growth rate in the $j - \alpha$ plane it was not possible to capture the stability boundary within the domain. Note that the discharge is becoming more stable at larger values of j. Due to the effect of j on magnetic shear s this indicates that the plasma might approach the second region of ballooning stability in this region. It is expected that the stability threshold moves closer to the experimental point as soon as two-fluid effects are considered, which is reserved for a future study.

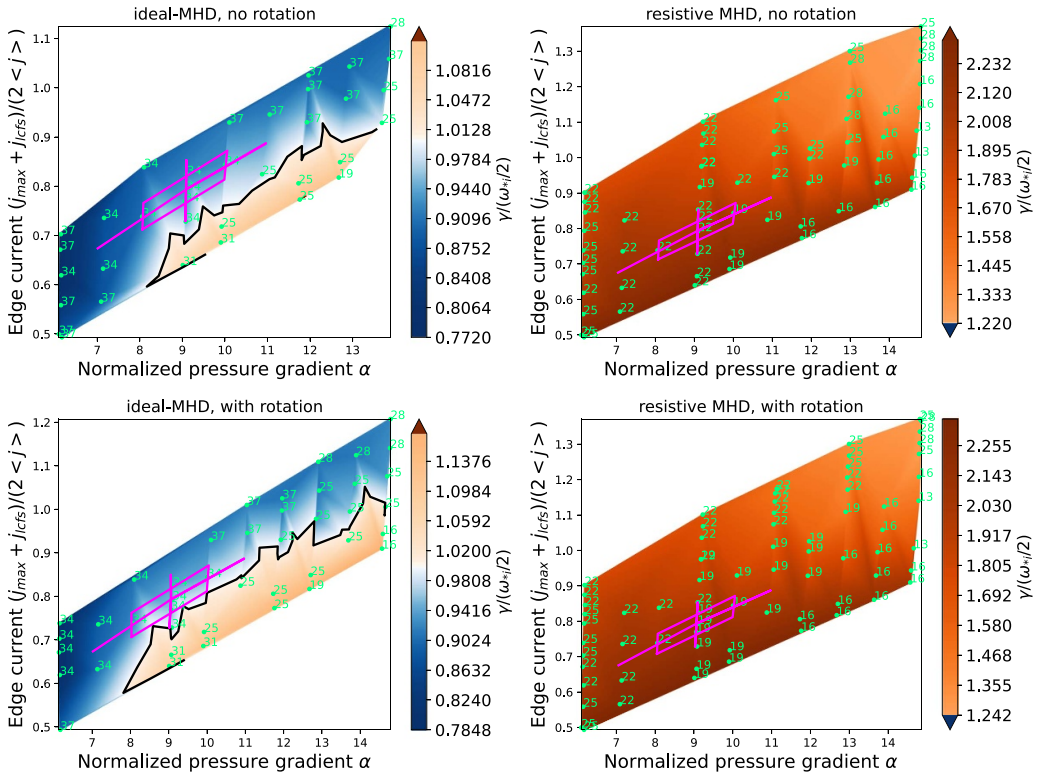

Figure 6. Peeling–ballooning stability boundary and normalized growth rate $\gamma/(\omega_{*i}/2)$ of the most unstable mode calculated for MAST-U pulse 45 272. The top row shows the results without equilibrium rotation, and the bottom row using the toroidal rotation profile without the diamagnetic term (orange curve in figure 4). (left) ideal-MHD. (right) resistive MHD.

Note that in the calculations based on the Spitzer resistivity model the experimental point is somewhat deep inside the unstable region. As the pedestal builds up during an ELM cycle the plasma usually is expected to develop an ELM once it passes the stability boundary. It is thus not yet clear why in the resistive calculations the experimental point is not closer to the stability limit. Even though our model considers more physical effects than ideal-MHD it still does not consider full two-fluid effects. Gyroviscosity, for example, can have an additional stabilizing effect as shown in [9]. The results nevertheless show that resistivity has a major impact on the stability limits, and the development of a more refined model including thoroughly measured rotation profiles is subject to future study.

4. Conditions for resistive PB modes

In this section we analyze the condition under which resistive PB modes are observed across the STs MAST, MAST-U and NSTX, but also a 'NSTX similarity' discharge in DIII-D, which adopts some NSTX-like parameters.

4.1. PB stability in 'NSTX similarity' discharge on DIII-D

A series of experiments has been performed on DIII-D, which aimed at achieving NSTX-like conditions [42]. While these discharges had major and minor radii typical for DIII-D, the toroidal magnetic field B_t, plasma current I_p, normalized beta β_N and shaping parameters (elongation κ, triangularity δ) were in the range that was typically achieved on NSTX. Given that ideal PB modes are seen on DIII-D, and resistive PB modes on NSTX, a discharge that uses some parameters from each device can provide a more comprehensive understanding of the conditions leading to unstable resistive edge modes. For this study, we select DIII-D discharge 140 996, which exhibits type-I ELMs and has a toroidal field of $B_t = -0.584$ T, plasma current of $I_p = 0.637$ MA, normalized β of $\beta_N = 3.277$, triangularity of $\delta = 0.556$ and $\kappa = 1.873$. The aspect ratio in this discharge is $A = 2.77$, which is about double the values on NSTX where $A \approx 1.2 - 1.5$. A fully kinetic equilibrium reconstruction was performed at 2517 ms with a window of 600 ms. As this is a free-boundary equilibrium we are able to include the inner wall of DIII-D in the computational domain. The flux surfaces of the reconstructed plasma are shown in figure 7(a), and the D_α signal in figure 7(b). This discharge has a wider pedestal than most other discharges on DIII-D, and in fact the pedestal width is in the range of type-I ELMy H-mode discharges on NSTX.

As for the MAST/-U cases above we calculate the peeling–ballooning stability limit in the ideal-MHD limit and with the resistive model. The results are presented in figure 8. The plasma appears unstable to PB modes in the ideal-MHD model with the experimental point being localized on the ballooning side. Plasma resistivity has a negligible effect on the growth rates and does not considerably shift the stability boundary. Thus, as in other conventional DIII-D discharges the type-I ELMs in this 'NSTX similarity' discharge are also associated with ideal PB modes.

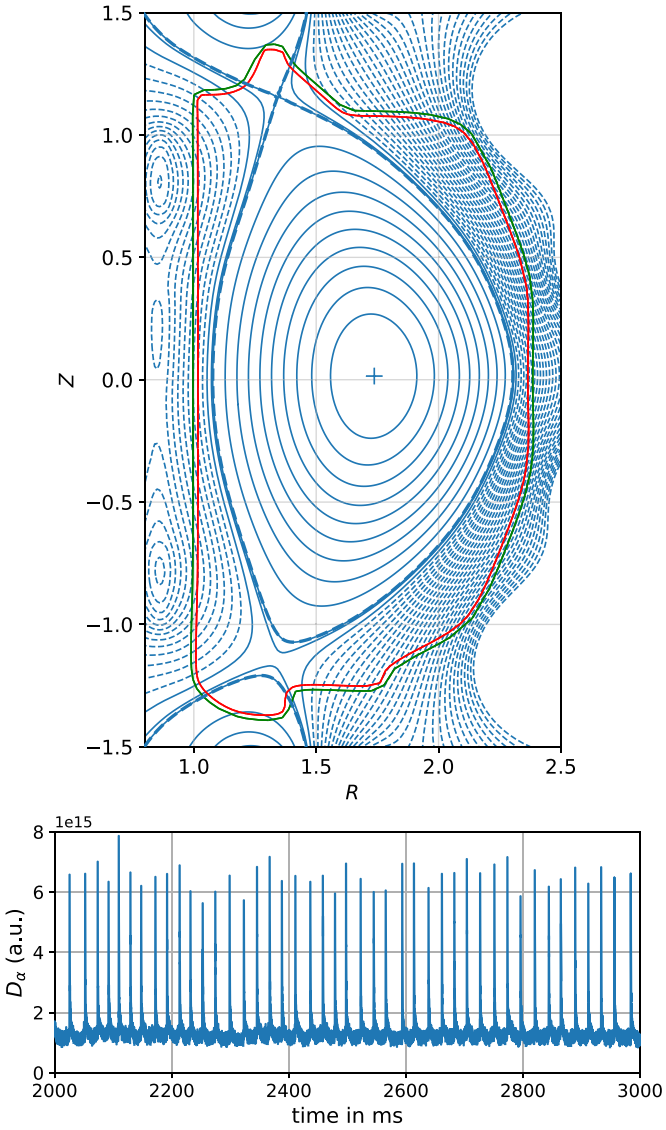

Figure 7. Equilibrium of DIII-D discharge 140 996, which has some NSTX-like parameters. (a) Equilibrium shape. (b) D_α signal showing the presence of type-I ELMS.

4.2. Discussion of physics associated with resistive PB modes

Table 1 lists scalar plasma parameters in ELMing discharges on MAST, MAST-U, NSTX and DIII-D in which PB stability was analyzed with resistive MHD models in M3D-C1. This is the entire set of ELMing discharges that were analyzed with M3D-C1. The NSTX discharges were chosen based physical relevance: cases with weaker and strong shaping and good quality equilibrium reconstructions. The MAST case was chosen as it showed clear type-I ELMs, and good measurements in the last 20% of the ELM cycle. Given the limitations of EFIT++ we were able to reconstruct an equilibrium with self-consistent pressure profiles, which is not guaranteed for all pulses on MAST. The MAST-U pulse was chosen as it was recently studied with ELITE and the results indicated that additional physics could play a role. The DIII-D discharge is a type-I ELMing discharge from a later campaign, where better diagnostics were available than in earlier campaigns. For each discharge the table states how strongly PB modes scale with resistivity. The quantities listed include parameters related to plasma shaping (aspect ratio A, elongation κ, triangularity δ), global parameters (β_N, q_{95}), which directly affect MHD stability, as well as pedestal parameters collisionality ν_*, ballooning parameter α, normalized current density[5] j^N_{ELITE} and pressure pedestal width w_{ped} and height h_{ped}. These parameters are expected to have the potential to affect PB stability. There is no clear correlation between the resistive scaling and any of the geometrical quantities, nor the pedestal parameters nor β_N. In particular, it can be asserted that resistive destabilization of PB modes is not directly linked to the aspect ratio of the plasma. However, $q_{95} > 6$ for discharges where an effect of resistivity on PB modes is observed and well below this value when there is a weak influence of resistivity. It should also be noted that modes in the peeling-limited regime appear to be more sensitive to resistivity than modes on the ballooning-limited side[6]. However, this observation is based on a limited amount of discharges, and needs to be confirmed further by simulations of additional discharges.

The most prominent physical effect introduced in our extended-MHD model compared with ideal-MHD is plasma resistivity, as discussed. In the Spitzer resistivity model, plasma resistivity $\eta \propto T_e^{-3/2}$, which suggests that either resistivity itself or electron temperature could directly correlate with the occurrence of unstable resistive peeling–ballooning modes. These and other normalized and non-normalized profiles are shown in figure 9 for all of the (ELMing) discharges that are listed in table 1. The color coding indicates how strongly the mode growth rates change when going from the ideal-MHD limit to Spitzer resistivity for each discharge. Red indicates a strong resistive scaling and a discharge that is limited by resistive modes, yellow indicates a discharge that shows a resistive scaling of medium intensity, and green indicates a weak resistive scaling, where Spitzer resistivity only marginally destabilizes the modes. Surprisingly, neither T_e nor η in the pedestal region seem to be connected to the observation of resistive edge modes. Nor do the profiles of electron density n_e, total pressure p and flux-averaged current density have an influence. Furthermore, it can be seen that neither the electron density normalized w.r.t. the Greenwald density limit n_e/n_G, the ballooning parameter α nor the Lundquist number S correlate with the impact of resistivity on the growth

[5] The normalized current density is defined as $j^N_{\mathrm{ELITE}} = \frac{j^{\mathrm{max,ped}}_{\mathrm{ELITE}} + j^{\mathrm{sep}}_{\mathrm{ELITE}}}{2j_{\mathrm{avg}}}$ with $j_{\mathrm{ELITE}} = \frac{f}{R_0}\left\langle \frac{\mathbf{j}\cdot\mathbf{B}}{B^2} \right\rangle$ and $j_{\mathrm{avg}} = I(\psi)/A(\psi)$, where $j^{\mathrm{max,ped}}_{\mathrm{ELITE}}$ is the maximum value of j_{ELITE} in the pedestal region, $j^{\mathrm{sep}}_{\mathrm{ELITE}}$ is the value of j_{ELITE} at the separatrix, $f = RB_\phi$, and $A(\psi)$ is the cross sectional area.

[6] This is shown in figure 3(b), where at high S, i.e. when moving from the ideal-MHD limit to Spitzer resistivity, the scaling is much stronger in the peeling-limited NSTX case than in the ballooning-limited MAST-U case.

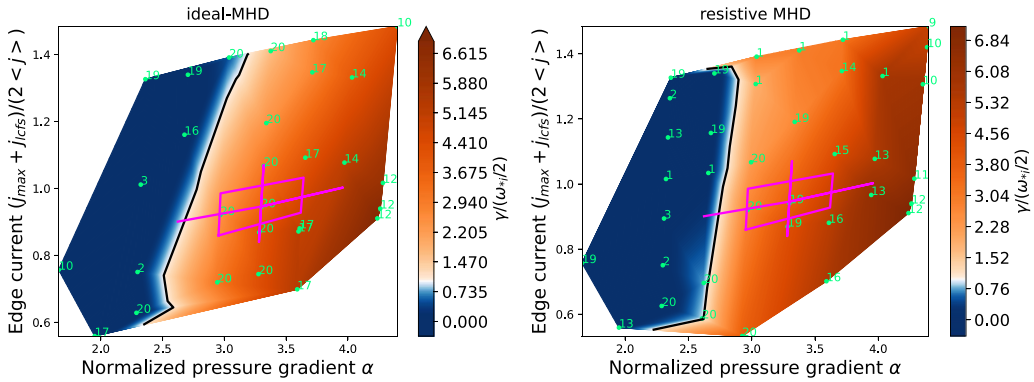

Figure 8. Normalized growth rate $\gamma/(\omega_{*i}/2)$ of the most unstable mode calculated with M3D-C1. The peeling–ballooning stability boundary $\gamma/(\omega_{*i}/2) = 1$ is shown as black line. The numbers denote the most unstable toroidal mode at each location. (a) ideal-MHD limit. (b) resistive MHD.

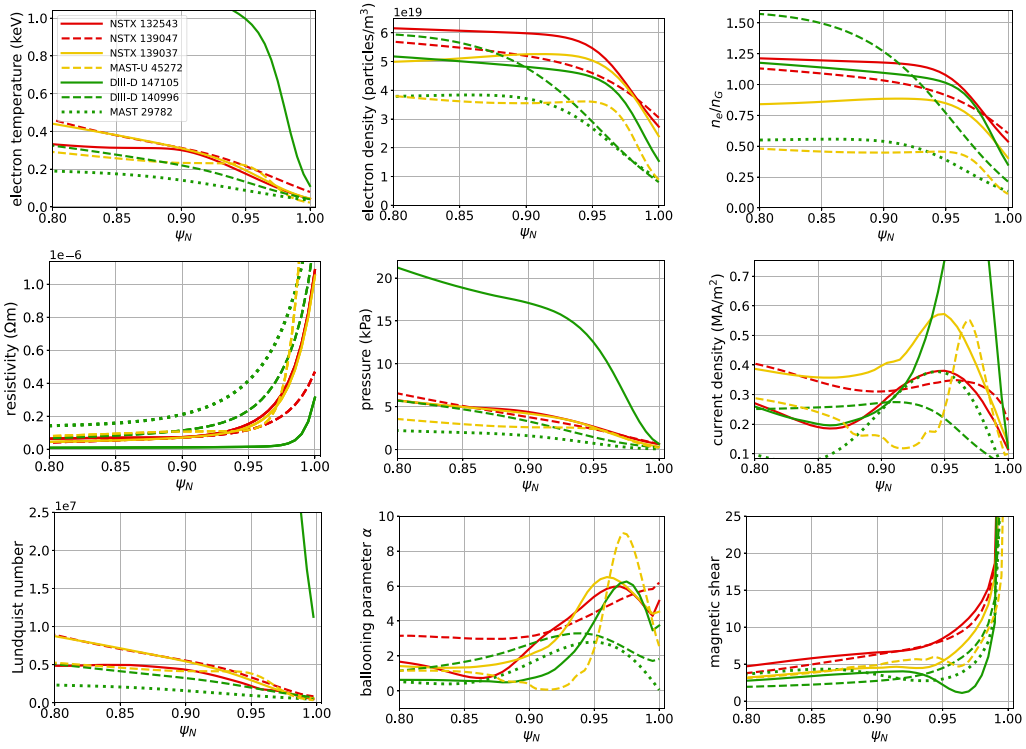

Figure 9. Different flux-averaged quantities are shown for ELMing discharges investigated on NSTX, MAST/-U and DIII-D with M3D-C1. The colors indicate how strongly the PB growth rates change when going from the ideal-MHD limit to Spitzer resistivity in each discharge. red: strong resistive scaling, yellow: medium resistive scaling, green: weak/no resistive scaling.

rates[7]. These normalized quantities might allow for a better inter-machine comparison. Note that the Lundquist number on DIII-D discharge 147 105 is considerably higher than for the other shown discharges and is partially excluded from the plot to better show the comparison for the remaining profiles. A clear correlation can, however, be seen between how resistivity impacts PB stability and the magnetic shear in the pedestal. How strong the effect of resistivity is, i.e. how the colors in figure 9 are chosen, is determined based on how strongly the stability boundary shifts in the $j - \alpha$ plane in between the ideal-MHD limit and the Spitzer resistivity models. While the current study shows a total of three discharges in MAST, MAST-U and DIII-D, the stability boundaries for the remaining discharges listed in table 1 and shown in figure 9 can be found in [8, 9]. A 'strong' effect of resistivity (red lines) exists when there is a transition from stability to instability

[7] The Lundquist number S can by itself have an effect on the growth rates as evidenced by the results in figure 3. When these resistive scalings are determined only S is scaled in an isolated manner, while other plasma parameters are held constant. On the other hand figure 9 shows the S profiles of several discharges with different overall configurations. This shows that the absolute value of S when compared among different discharges does not determine whether resistive PB modes are observed in said discharge. For sufficiently high values of S it would be expected that the growth rates approach those of ideal modes. However, the given discharges do not lie within this asymptotic regime.

Table 1. Scalar parameters taken at the time of the equilibrium reconstruction in ELMing discharges on various devices and how they correlate with the resistive scaling.

device	NSTX	NSTX	NSTX	MAST-U	DIII-D	DIII-D	MAST
discharge	132 543	139 047	139 037	45 272	147 105	140 996	29 782
	peeling	peeling	ballooning	ballooning	PB corner	ballooning	ballooning
scaling	strong	strong	medium	medium	weak	weak	weak
$A = a/R$	1.37	1.45	1.27	1.57	3.05	2.77	1.47
elongation κ	2.10	2.31	2.38	2.10	1.82	1.81	1.60
triangularity δ	0.538	0.626	0.572	0.454	0.542	0.486	0.325
β_N	5.241	5.466	4.318	2.23	2.371	3.28	3.07
q_{95}	7.347	8.000	6.470	6.11	3.563	2.55	3.62
ν_*	0.6201	0.6456	0.3748	0.7406	0.1256	0.7196	0.8227
α	6.003	6.086	6.477	8.8	6.314	3.29	2.796
j_{ELITE}	0.544	0.641	0.699	0.787	1.700	0.448	0.550
w_{ped} (p_{total}) in ψ_N	0.1191	0.1098	0.0829	0.046	0.0614	0.157	0.118
h_{ped} (p_{total}) in Pa	4933.61	2318.19	3852.20	2232.29	14 965.82	4811.15	1797.27

at the experimental point together with a considerable expansion of the unstable domain. A 'medium' effect is characterized by the existence of some form of instability at the experimental point in ideal-MHD (such as seen in figure 2), but at the same time the unstable domain increases in size considerably. A 'weak' effect of resistivity is seen when there is only a negligible shift of the stability threshold in $j - \alpha$ space between the ideal-MHD and resistive calculations. The correlation with magnetic shear together with the influence of q_{95} on resistive modes indicate that the safety factor in the pedestal region plays a much stronger role in triggering resistive PB modes than thermal quantities such as T_e, p and even plasma resistivity itself, whether they are taken in absolute values or normalized.

5. Conclusions

In this study we investigated whether resistive peeling–ballooning modes can occur in MAST and MAST-U, and we calculated the stability boundaries using single fluid extended-MHD and an ideal-MHD limit for comparison. Simulations were performed with and without equilibrium flows. The sensitivity of the PB growth rate to resistivity was investigated, and a comparison was performed with the NIMROD code to increase confidence in the M3D-C1 results. The results confirm previous ideal-MHD PB thresholds calculated with ELITE on MAST prior to the upgrade. In MAST-U, we find resistive PB modes similar to those seen on NSTX [8]. Resistive PB in MAST-U appear to have more dominant ballooning features compared with NSTX. In the ideal-MHD limit the simulations with M3D-C1 recover a PB stability threshold that is similar to that found by ELITE. While in the ELITE calculations the stability threshold had to be arbitrarily chosen [16], the present M3D-C1 simulations use a widely accepted threshold based on the diamagnetic frequency [24, 43–48]. The main benefit of using M3D-C1 over ideal-MHD codes is the inclusion of non-ideal effects, and as shown in the present study, plasma resistivity can matter in the destabilization of macroscopic modes in the pedestal. Simulations including equilibrium flow were carried out, but at least on MAST and MAST-U its effect on PB stability seems negligible. We also investigated the conditions that trigger resistive PB modes by correlating scalar plasma parameters and plasma profiles with the intensity of the resistive scaling of PB modes. For this analysis we chose discharges from MAST, MAST-U, NSTX and DIII-D that have so far been studied with M3D-C1 in the context of resistive peeling–ballooning modes. It is found that the edge magnetic shear correlates well with the sensitivity of PB modes to plasma resistivity, whereas resistivity itself, or shaping parameters are uncorrelated among other quantities. The results show that resistive peeling–ballooning modes can appear in more plasma conditions in various machines than previously described. While the extended-MHD model employed in M3D-C1 to study peeling–ballooning stability still has limitation, such as not including full two-fluid effects or neoclassical corrections, it is effective in capturing PB stability thresholds, where ideal-MHD models struggled. In all cases that have been studied so far in previous work [8, 9] and in the current study, the M3D-C1 single-fluid model consistently predicted ELMing plasmas to be in the PB-unstable domain, and ELM-free discharges on the stable side. This provides an improvement over pure ideal-MHD models that sometimes fail to do so. Future work will be focused on improving the model further in order to obtain stability thresholds that are closer to the experimental point as would be expected based on the idea of pedestal evolution (pedestal build-up until stability threshold is hit upon ELM-crash). This will be done by including gyroviscous stress (expected to be stabilizing), neoclassical and

Z_{eff} corrections to resistivity (expected to be destabilizing), as well as Hall terms (expected to be stabilizing). Current work with NIMROD and M3D-C1 is ongoing to refine the extended-MHD model in order to obtain stability thresholds that lie closer to the experimental points by including finite-Larmor radius and two-fluid effects. This will be reported in a future publication.

Data availability statement

The data that support the findings of this study are openly available at the following URL/DOI: https://doi.org/10.34770/emxt-0v05 [49].

Acknowledgments

The authors would like to thank Brian Grierson, Florian Laggner, Siobhan Smith, Bhavin Patel, Tanmay Macwan and Mate Lampert for useful discussion. This work was supported by the U.S. Department of Energy SciDAC program under Award Number DE-AC02-09CH11466 in the Center for Edge of Tokamak Optimization (CETOP) and the Department of Energy early career research program. This material is based upon work supported by the U.S. Department of Energy, Office of Science, Office of Fusion Energy Sciences, using the DIII-D National Fusion Facility, a DOE Office of Science user facility, under Award(s) DE-FC02-04ER54698. This work has been part-funded by the EPSRC Energy Programme [Grant Number EP/W006839/1]. The United States Government retains a non-exclusive, paid-up, irrevocable, world-wide license to publish or reproduce the published form of this manuscript, or allow others to do so, for United States Government purposes.

ORCID iDs

A Kleiner 0000-0002-5800-8027
K Imada 0000-0002-8128-2438
N M Ferraro 0000-0002-6348-7827
S R Haskey 0000-0002-9978-6597

References

[1] Leonard A W 2014 *Phys. Plasmas* **21** 090501
[2] Groebner R J and Saarelma S 2023 *Plasma Phys. Control. Fusion* **65** 073001
[3] Maingi R *et al* (the NSTX research team) 2009 *Phys. Rev. Lett.* **103** 075001
[4] Boyle D P, Maingi R, Snyder P B, Manickam J, Osborne T H, Bell R E and LeBlanc B P 2011 *Plasma Phys. Control. Fusion* **53** 105011
[5] Sontag A *et al* 2011 *Nucl. Fusion* **51** 103022
[6] Diallo A, Maingi R, Kubota S, Sontag A, Osborne T, Podestà M, Bell R, LeBlanc B, Menard J and Sabbagh S 2011 *Nucl. Fusion* **51** 103031
[7] Diallo A *et al* 2013 *Nucl. Fusion* **53** 093026
[8] Kleiner A, Ferraro N, Diallo A and Canal G 2021 *Nucl. Fusion* **61** 064002
[9] Kleiner A, Ferraro N, Canal G, Diallo A and Maingi R 2022 *Nucl. Fusion* **62** 076018
[10] Berkery J *et al* 2024 *Nucl. Fusion* **64** 112004
[11] Nyström H, Frassinetti L, Saarelma S, Huijsmans G, von Thun C P, Maggi C and Hillesheim J (JET contributors) 2022 *Nucl. Fusion* **62** 126045
[12] Pamela S *et al* 2017 *Nucl. Fusion* **57** 076006
[13] Pamela S J P, Huysmans G T A, Beurskens M N A, Devaux S, Eich T and Benkadda S (JET EFDA contributors) 2011 *Plasma Phys. Control. Fusion* **53** 054014
[14] Xu X, Dudson B, Snyder P, Umansky M, Wilson H and Casper T 2011 *Nucl. Fusion* **51** 103040
[15] Ebrahimi F and Bhattacharjee A 2023 *Nucl. Fusion* **63** 126042
[16] Imada K, Osborne T, Saarelma S, Clark J, Kirk A, Knolker M, Scannell R, Snyder P, Vincent C and Wilson H (the MAST Upgrade Team) 2024 *Nucl. Fusion* **64** 086002
[17] Jardin S 2004 *J. Comput. Phys.* **200** 133–52
[18] Sovinec C, Glasser A, Gianakon T, Barnes D, Nebel R, Kruger S, Schnack D, Plimpton S, Tarditi A and Chu M 2004 *J. Comput. Phys.* **195** 355–86
[19] Aiba N, Pamela S, Honda M, Urano H, Giroud C, Delabie E, Frassinetti L, Lupelli I, Hayashi N and Huijsmans G (the JET Contributors and JT-60SA Research Unit) 2017 *Plasma Phys. Control. Fusion* **60** 014032
[20] Breslau J, Ferraro N and Jardin S 2009 *Phys. Plasmas* **16** 092503
[21] Jardin S, Breslau J and Ferraro N 2007 *J. Comput. Phys.* **226** 2146–74
[22] Ferraro N M, Jardin S C and Snyder P B 2010 *Phys. Plasmas* **17** 102508
[23] Artola F J, Sovinec C R, Jardin S C, Hoelzl M, Krebs I and Clauser C 2021 *Phys. Plasmas* **28** 052511
[24] Snyder P, Groebner R, Hughes J, Osborne T, Beurskens M, Leonard A, Wilson H and Xu X 2011 *Nucl. Fusion* **51** 103016
[25] Hastie R J, Catto P J and Ramos J J 2000 *Phys. Plasmas* **7** 4561–6
[26] Huysmans G T A, Sharapov S E, Mikhailovskii A B and Kerner W 2001 *Phys. Plasmas* **8** 4292–305
[27] Knolker M, Osborne T, Belli E, Henderson S, Kirk A, Kogan L, Saarelma S and Snyder P 2021 *Nucl. Fusion* **61** 046041
[28] Berkery J W, Sabbagh S A, Kogan L, Ryan D, Bialek J M, Jiang Y, Battaglia D J, Gibson S and Ham C 2021 *Plasma Phys. Control. Fusion* **63** 055014
[29] Appel L and Lupelli I 2018 *Comput. Phys. Commun.* **223** 1–17
[30] Meneghini O and Lao L 2013 Integrated modeling of tokamak experiments with OMFIT *Plasma Fusion Res.* **8** 2403009
[31] Meneghini O *et al* 2015 Integrated modeling applications for tokamak experiments with OMFIT *Nucl. Fusion* **55** 083008
[32] Osborne T H, Snyder P B, Burrell K H, Evans T E, Fenstermacher M E, Leonard A W, Moyer R A, Schaffer M J and West W P 2008 *J. Phys.: Conf. Ser.* **123** 012014
[33] Lütjens H, Bondeson A and Sauter O 1996 *Comput. Phys. Commun.* **97** 219–60
[34] Kleiner A, Graves J, Cooper W, Nicolas T and Wahlberg C 2018 *Nucl. Fusion* **58** 074001
[35] Roberts K V and Taylor J B 1962 *Phys. Rev. Lett.* **8** 197–8
[36] Gryaznevich M *et al* (the MAST Team) 2008 *Nucl. Fusion* **48** 084003
[37] Chapman I, Hua M-D, Pinches S, Akers R, Field A, Graves J, Hastie R and Michael C (the MAST Team) 2010 *Nucl. Fusion* **50** 045007
[38] Saarelma S, Hender T C, Kirk A, Meyer H and Wilson H R (MAST Team) 2006 *Plasma Phys. Control. Fusion* **49** 31

[39] Kirk A , O'Gorman T, Saarelma S, Scannell R and Wilson H R 2009 *Plasma Phys. Control. Fusion* **51** 065016
[40] Snyder P 2020 Private communication
[41] Sykes A, Bishop C M and Hastie R J 1987 *Plasma Phys. Control. Fusion* **29** 719
[42] Burrell K, Grierson B, Solomon W and Belli E 2014 *Nucl. Fusion* **54** 083020
[43] Snyder P B, Groebner R J, Leonard A W, Osborne T H and Wilson H R 2009 *Phys. Plasmas* **16** 056118
[44] Burrell K, Osborne T, Snyder P, West W, Fenstermacher M, Groebner R, Gohil P, Leonard A and Solomon W 2009 *Nucl. Fusion* **49** 085024
[45] Wade M *et al* 2015 *Nucl. Fusion* **55** 023002
[46] Saarelma S, Challis C D, Garzotti L, Frassinetti L, Maggi C F, Romanelli M and Stokes C (JET Contributors) 2017 *Plasma Phys. Control. Fusion* **60** 014042
[47] Fenstermacher M *et al* 2025 *Nucl. Fusion* **65** 053001
[48] Frassinetti L *et al* 2025 *Nucl. Fusion* **67** 075011
[49] Kleiner A, Imada K, Ebrahimi F, Ferraro N, Haskey S, Kogan L and Pankin A 2025 Data for "A study of resistive peeling-ballooning modes across spherical tokamaks" (Princeton Plasma Physics Laboratory) (https://doi.org/10.34770/emxt-0v05)